ACS APPLIED MATERIALS & INTERFACES

Research Article

Cite This: ACS Appl. Mater. Interfaces 2019, 11, 11238−11250

www.acsami.org

High-Throughput 2D Heteroatom Graphene Bioelectronic Nanosculpture: A Combined Experimental and Theoretical Study

Adeniyi Olugbenga Osikoya,[†] Francis Opoku,[†] Ezekiel Dixon Dikio,*[,‡] and Penny Poomani Govender*[,†]

[†]Department of Applied Chemistry, University of Johannesburg, P.O. Box 17011, Doornfontein 2028 Johannesburg, South Africa

[‡]Applied Chemistry and Nanoscience Laboratory, Department of Chemistry, Vaal University of Technology, P.O. Box X021, 1900 Vanderbijlpark, South Africa

Supporting Information

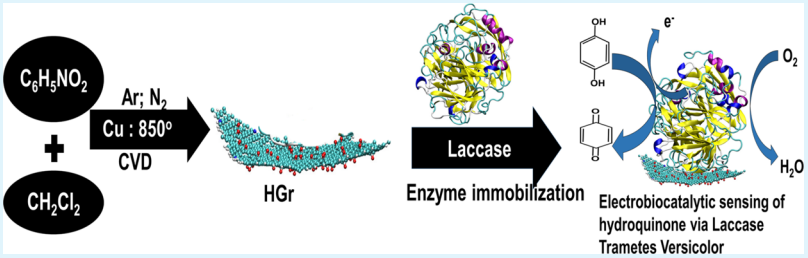

ABSTRACT: In this study, chemical vapor deposition-synthesized heteroatom graphene (HGr) bioelectronic interfaces have been developed for ultrafast, all-electronic detection and analysis of molecules by driving them through tiny holes—or atompores—in a thin lattice of the graphene sheet, including the efforts toward facilitating enhanced electrocatalytic and mapping electron transport activities. The presence of chlorine, nitrogen, and oxygen in the crystalline graphitic layers (<7) has been confirmed using Raman spectroscopy, X-ray photoelectron spectroscopy, and high-resolution transmission electron microscopy. We report a swift bioelectrocatalytic response to step-by-step additions of the substrate with the achievement of a steady current within a few seconds. The response limit was 2.07 μM with a dynamic range of sensing from 2.07 μM to 2.97 mM. The electronic properties and adsorption energies of hydroquinone and *p*-benzophenone molecule adsorption on pristine, O-, N-, and Cl-doped graphene nanosheet surfaces were systematically investigated using first-principles calculations. The results revealed that the adsorption capacity was improved upon doping graphene nanosheets with O, N, and Cl atoms. Hence, Cl-doped graphene nanosheets were shown as a promising adsorbent toward hydroquinone and *p*-benzophenone detection.

KEYWORDS: *heteroatom graphene, XPS, laccase, computational studies, electrobiocatalysis, DFT, biosensor*

INTRODUCTION

Considering the insightful impact of electronics on biomedical applications in the past, it is just simple to concoct that, incorporation of up-to-the-minute smart bioelectronic interfaces will result in profound quantum leaps. Continuous efforts in the miniaturization of electronic biodevices are leading to new openings in biomedical research and translational medical applications.[1]

The dimensions and length scale of architectures that can steadfastly be fabricated by means of nanotechnology are now adequately tiny that novel devices can be envisaged to investigate in vitro or in vivo.[2] Advanced integration of two-dimensional (2D) materials and architecting of the electronic circuitry can be assimilated with diverse precise sensors, actuators, and biocomputers to enable the creation of biodevices and bioelectronic interfaces that can intelligently probe biotic organizations from molecules to cells to whole organism levels and thus unfold the landscape of fundamental biocatalytic research and novel opportunities for advanced translation. Exceedingly incorporated high-throughput bioelectronic interfaces create possibilities of smart implantable biodevices that can sense their precise microenvironment and dynamically prefer an appropriate response, as in intelligent 2D drug-delivery chips. Numerous other purposes transpire from the sustained integration of high-throughput 2D interfaces with bioelectronics that will result in new revolutionary biomedical advances.[3] Development of atomic-scale 2D high-throughput bioelectronics will be an enabler for the future maturity of molecular-based personalized medicine.[4,5]

Graphene and its derivatives (such as graphene oxide, reduced graphene oxide, and doped graphene among others) have recently been attracting considerable attention from researchers and material scientists as choice materials for device fabrication because of its outstanding mechanical strength, electronic transport properties, and biocompatibility.[6−10] Consequently, graphene and its derivatives have found

Received: February 4, 2019
Accepted: February 28, 2019
Published: February 28, 2019

DOI: 10.1021/acsami.9b01914
ACS Appl. Mater. Interfaces 2019, 11, 11238−11250

applications in highly sensitive, thin, flat, and flexible smart devices including in bioreactors, biosensors, bioelectronics, supercapacitors, energy storage, and biofuel cells and as graphene transistors in logic gate devices.[8,10−12]

In this kernel, the development of atom-thick, inserted heteroatom graphene as an electron wire between the biomolecule and the electrode surface will enhance high-class electrocatalytic implementation because of the synergistic effect of the essential heteroatoms in providing active spots for superior electron mobility and communication within the integrated system.[13] Therefore, it is now the need of the hour to develop and fabricate an appropriate super-thin probe aimed at facilitating ultramodest bioelectronics.[14] Deliberate insertion of heteroatoms in the 2D lattice of the graphene sheet alters the electrocatalytic properties of graphene and consequently enhances the biocatalytic properties of the 2D plane via electrostatic attraction and compatibility with oppositely charged biomolecules.[1,15] Furthermore, the point of insertion of the heteroatoms creates additional active polar spots in the inert pristine graphene planes[16,17] while largely conserving its sp^2-hybridized architecture as well as consequently maintaining the fast electron-transfer property.[18] The active sites are quite important for enhancing efficient electron transfer between the active sites of the biomolecules and the electrode surfaces.

Heteroatom graphitic carbon has been reported with higher catalytic activity and greater stability than the monoatom-doped variant of the same graphitic carbon material (R). Higher catalytic activity of dually (N and P) doped 2D graphene is attributed to the synergistic effects of the doped nitrogen and phosphorus atoms, the full and efficient use of the active site decorated by the doped nitrogen and phosphorus atoms, the higher conductivity of graphene, the larger surface area, and the more hierarchical pores enhancing the sufficient contacts with nitrogen and phosphorus toward oxygen reduction reaction and oxygen evolution reaction.[18,19]

Herein, we have optimized a chemical vapor deposition (CVD)-based method under an inert atmosphere comprising a mixture of argon (Ar) and nitrogen (N) gases at 850 °C by using a mixture of dichloromethane (CH_2Cl_2) and nitrobenzene ($C_6H_5NO_2$) as carbon source and dopant sources, respectively. The doped graphene nanosculpture was characterized by transmission electron microscopy (TEM), X-ray photoelectron spectroscopy (XPS), Raman spectroscopy, energy dispersive spectroscopy (EDS), X-ray diffraction (XRD) spectroscopy, and atomic force microscopy (AFM) methods. The high-throughput electrobiocatalytic activities have been examined with copper-containing oxidase enzyme laccase as a biocatalyst to perform a one-electron oxidation through impedimetric and amperometric measurements.

Density functional theory (DFT) is broadly employed for the examination of electronic properties and structural stability assessments of several types of molecules.[20,21] In this study, DFT calculation was employed to investigate the adsorption energy and characteristics of hydroquinone and *p*-benzophenone molecule adsorption on the pristine, O-, N-, and Cl-doped graphene nanosheets. Moreover, density of states (DOS), charge density difference (CDD), work function, and Hirshfeld charge analysis were also used to examine the doping effect of O, N, and Cl elements on the atomic structures, adsorption properties, and performance.

EXPERIMENTAL SECTION

Chemicals. Nitrobenzene ($C_6H_5NO_2$, 99.5%, Labchem, South Africa), dichloromethane (CH_2Cl_2, 99%, Labchem, South Africa), argon (Ar, 99.999%, Afrox, Gauteng, South Africa), nitrogen (N_2, 99.99%, Afrox, Gauteng, South Africa), ethanol (C_2H_5OH, 99%, Labchem, South Africa), and copper sheet (100% purity) in the size of 1 mm × 15.0 cm × 15.0 cm (thickness × width × length, Labchem, South Africa) were used. Laccase from *Trametes versicolor* (100 U/mg), potassium dihydrogen phosphate monobasic (KH_2PO_4) (99.99%), dipotassium hydrogen phosphate (K_2HPO_4) (≥99%), potassium chloride (KCl) (≥99%), ferrocene carboxylic acid (97%), and poly(3,4-ethylenedioxythiophene)-poly(styrenesulfonate) (PEDOT-PSS) (≥99%) were purchased from Sigma-Aldrich (St. Louis, MO, USA) and used as received. Acetic buffer (1×, pH 4.9) and ferrocene carboxylic acid aqueous solutions were used as the supporting electrolyte for amperometric cyclic voltammetry (CV) measurements. Aqueous solutions were prepared with double-distilled water from a Millipore system (18.2 MΩ cm).

2D Nanosculpture Heteroatom Graphene Synthesis. The CVD-synthesized HGr was deposited on a copper sheet (1 mm thickness and 2.0 × 6.0 cm) after extensively cleaning the copper with absolute ethanol. The experimental procedure involved placing a metal strip right into the middle of a horizontal quartz tube, which was then inserted into a Nabertherm P330 furnace with a digital and programmable controller. A Teledyne Power Pod 400 mass-flow controller was connected to the system via quartz glass connectors and rubber tubes. The deposition of HGr on the copper sheet was achieved using a mixture of argon (Ar) and nitrogen (N_2) as carrier gases at flow rates of 350 and 250 cm^3/min, respectively, while a mixture (ratio 1:1) of nitrobenzene ($C_6H_5NO_2$) and dichloromethane (CH_2Cl_2) was used as the carbon and dopant sources. The process involved purging the quartz tube with argon gas flowing at the rate of 50 cm^3/min for 30 min, after which the programmed temperature controller started heating the CVD system. The purge/carrier gas (argon) at the flow rates stated earlier were introduced into the system to purge the CVD tube of air and create an inert atmosphere in preparation for the reaction; after the attainment of the respective synthesis temperatures, the system was allowed to stabilize under the continuous argon flow at 400 cm^2/min for 10 min before the commencement of the reaction. The synthesis reaction was started by bubbling the nitrogen gas (at the flow rate of 250 cm^3/min) for 2 min through the mixture of nitrobenzene and dichloromethane and ended by stopping the nitrogen gas flow. The reaction products were allowed to cool to 500 °C under the inert gas mixture of Ar and N_2, and they were then cooled at room temperature (RT) under argon gas flow (alone) at a flow rate of 50 cm^3/min. The experimental CVD schematic setup is presented in Figure S1 (Supporting Information), while the representative equation for the reaction is presented in Figure S2 (Supporting Information).

Characterization. All electrochemical measurements (CV, amperometry and impedimetry) were carried out with an Ivium Stat.XR electrochemical analyzer (Eindhoven, The Netherlands). The electrochemistry experiments were performed using a three-electrode cell comprising of a glassy carbon electrode (GCE) with a surface area of 0.07 cm^2 as the working electrode, Ag/AgCl in 3 M KCl as the reference electrode, and a platinum auxiliary wire as the counter electrode. The zeta potential of the HGr graphene dispersions was measured using a Nano ZS dynamic light-scattering-zeta potential measuring instrument (Malvern Instruments, Worcestershire, UK). TEM was performed by using the Linköping University double-corrected high brightness Titan3 60-300 scanning transmission electron microscope. Electron microscopy was performed at 60 kV using a monochromated beam, with better than 200 meV full width at half-maximum energy resolution, for a final point resolution around 1 Å. The materials for TEM characterization were prepared by dispersing 1 mg of the doped heteroatom graphene in 10 mL of polyelectrolyte interface (PI) solution (1%), and the mixture was sonicated for 30 s to ensure even dispersion. Then, 5 μL of the sample

DOI: 10.1021/acsami.9b01914
ACS Appl. Mater. Interfaces 2019, 11, 11238−11250

solution was dropped on a 3 μm copper grid (Agar Scientific, Essex, UK) and left to dry at RT in the fume hood for 24 h.

Theoretical Studies. We have carried out computational modeling to understand the interaction between HGr and laccase enzyme in comparison to plain graphene. A simple model for graphene (with 6 × 5 units) was used, and the graphene edge atoms (or the dangling bonds) were capped with hydrogen atoms. HGr was prepared using the simple graphene model by substituting the carbons and hydrogens with nitrogen and chloride atoms according to EDS and XPS results. Further epoxy groups were added on both sides of the graphene. As mentioned before, the number of nitrogen, chlorine, and oxygen atoms used for preparing the model HGr was based on the experimental analysis and the report on the percentage of each of these atoms in HGr.

The structures of graphene and HGr were optimized on the PM6 semiempirical level of theory, and the computed Mulliken charges were used in the subsequent molecular dynamics (MD). The laccase enzyme structure was based on the XRD structure reported in the protein database (reference number 1KYA),[22] and the source of the enzyme was *T. versicolor,* as chosen in the experiment. To choose the right starting configuration for MD simulations, first, a blind docking was carried out while considering laccase as the receptor and graphene or HGr as the ligands. The most stable complex structures obtained for graphene-laccase and HGr-laccase from docking were used for subsequent MD simulations. Both graphene + laccase and HGr + laccase complex structures were solvated with approximately 30 000 water molecules and neutralized with 25 Na^+ ions. Approximately, 1% of the PEDOT:PSS mixture was used in experiments to improve the solubility of graphene. However, the simulations were carried out in water solvent alone as the model system mimicking an extremely dilute condition [we just have a single protein and substrate (graphene and HGr) dissolved in water solvent]. Because of the limitation with computational resources, the model with maximum probability was targeted to create a sufficient model to provide insight into the interaction between the graphene or HGr subsystem and the enzyme.[23]

The FF99SB force field was used to describe the enzyme, while the GAFF force field along with the charges obtained using the PM6 level of theory was used to describe graphene and HGr layers. The water solvent has been described using the TIP3P force field[24] as well. MD simulations were carried out using Amber12 software.[25] Three sets of simulations were carried out for the following systems: (i) laccase in water, (ii) graphene:laccase in water, and (iii) HGr:laccase in water. All simulations were carried out in an isothermal isobaric ensemble, which allows the system to reach the appropriate density. The time step for the integration of equation of motion was chosen as 2 fs. The temperature and pressure were assumed as RT and 1 atm, which were simulated by connecting the system to a Langevin thermostat and a Berendsen barostat, respectively. Initially, a minimization run was carried out followed by simulation at RT.

The simulations were carried out until the system energies and density converged, indicating that the system reached the equilibrium. Then, production run was carried out for 20 ns. The trajectories corresponding to the production runs were used for various analyses, including the calculation of the interaction energies between the graphene and HGr layers and the enzyme. Further, the secondary structure of the enzyme was analyzed for the three cases, namely, (i) laccase in water, (ii) laccase when bound to graphene, and (iii) laccase when bound to the HGr layer.

Computational Details. The structural, adsorption, and electronic properties of hydroquinone and *p*-benzophenone molecule adsorption on pristine, O-, N-, and Cl-doped graphene nanosheets were performed within the framework of plane-wave DFT using the Cambridge Serial Total Energy code[26] of Material Studio 2016 package.[27] The generalized gradient approximation with the Perdew–Burke–Ernzerhof functional[28] was employed as the exchange–correlation functional, and it was broadly used to account for the interactions between the adsorbate and substrate systems.[29,30] The ultrasoft pseudopotential by Vanderbilt[31] was used for the valence and core electronic interactions. The van der Waals forces were considered using the Tkatchenko and Scheffler correction.[32] To minimize the interlayer interaction, the vacuum space was set at 20 Å. The Brillouin zone was sampled via the Monkhorst–Pack *k*-point grid of 4 × 4 × 1.[33] The atomic positions were allowed to relax by the Broyden–Fletcher–Goldfarb–Shanno algorithm[34] until the energy, force, and displacement convergence criteria were less than 10^{-6} eV/atom, 0.3 eV/Å, and 0.01 Å, respectively.

To understand the doping effect on the adsorption properties of hydroquinone and *p*-benzophenone on the pristine, O-, N-, and Cl-doped graphene nanosheets, the adsorption energy was calculated and defined as follows

$$E_{ads} = E_{graphene+molecules} - E_{graphene} - E_{molecules}$$

where $E_{graphene+molecules}$ denotes the energy of the system with the hydroquinone and *p*-benzophenone molecules adsorbed onto graphene with or without O-, N-, and Cl-dopants, $E_{graphene}$ is the energy of graphene with or without the dopants, and $E_{molecules}$ is the energy of the adsorbate (hydroquinone and *p*-benzophenone molecules) in the same vacuum slab. The charge transfer was investigated using the Hirshfeld charge analysis.[35]

Development of High-Throughput Heteroatom Graphene Interface. The nanostructured high-throughput 2D heteroatom graphene–enzyme interface bioelectrode was prepared by dispersing 1.0 mg of as-synthesized HGr powders in 1 mL of aqueous PEDOT-PSS solution (1% by mass). The mixture was sonicated for 2h and incubated at RT under mild stirring conditions for further 3 h. After that, the resulting suspension was subjected to three centrifugation/resuspension (in PEDOT-PSS solution, 1% by mass) cycles to isolate the HGr agglomers.

The enzyme solution was prepared by dissolving 10 mg of laccase in 1 mL of acetate buffer solution (pH: 5.0, 0.1 M) in 0.1 M KCl. The enzyme solution was then incubated under mild stirring at RT for 3 h.

The conjugation of the enzyme with the dispersed HGr was achieved by mixing 500 μL of the dispersed heteroatom graphene, as described above, with 500 μL of the prepared enzyme solution, and the mixture was incubated at RT for 3 h.

Electrocatalytic Properties Study. First, GCEs were carefully precleaned and polished using a 1.0, 0.3, and 0.05 μm Buehler alumina slurry on Buehler polishing microcloths (Buehler, Ltd. USA) separately. The bioconjugate solution, which contained the dispersed heteroatom graphene and the enzyme, was homogenized by sonication for 1 min. This homogeneous HGr-laccase dispersion (20 μL) was drop-cast on the precleaned GCE surface and dried at 4 °C for 8 h. The other electrodes, such as with/without enzyme, were prepared using the same procedure described above.

RESULTS AND DISCUSSION

The total interaction energies between the graphene:laccase and HGr:laccase systems were computed, and the van der Waals and electrostatic contributions to the total energies were calculated. The results are presented in Table 1. The stabilizing

Table 1. Total Interaction Energies and Individual Contributions (Electrostatic and van der Waals) for Laccase + Graphene and Laccase + Hgr Hybrid Systems[a]

	E_{vdW}	E_{elec}	E_{total}
laccase + graphene	−288.0	41.5	−246.5
laccase + HGr	−287.5	21.8	−265.7

[a]The energies are in kcal/mol.

interaction of laccase with both graphene and HGr is dominated by the van der Waals type.[22] Moreover, the electrostatic interaction is destabilizing, which has to be attributed to the larger total charge of the enzyme (charge is −25 e). Overall, the laccase + HGr hybrid system is more stable than the laccase + graphene system by approximately 19

DOI: 10.1021/acsami.9b01914
ACS Appl. Mater. Interfaces 2019, 11, 11238–11250

kcal/mol, which is directly connected to increased immobilization of the enzyme on the Hgr surface than on the graphene surface.[36]

The secondary structure of laccase enzyme has been computed using the timeline analysis tool as implemented in VMD software[37] for the three cases of laccase (i.e., laccase alone in water and laccase in graphene and Hgr surfaces). The secondary structure for each of the aminoacids of the enzyme is characterized by single letter codes namely T, E, B, H, G, I, and C referring to turn, extended configuration, isolated bridge, α helix, 3-10 helix, π helix, and coil, respectively. We have computed the percentage population of each of the secondary structures using the data obtained from the timeline analysis, and the results are presented in Table 2. As can be seen, the secondary structure is significantly altered depending upon the nature of the surface. In the case of graphene, the beta sheet contents are reduced significantly (by 2%), whereas it increases by 0.8% in the case of the HGr surface.

Table 2. Average Secondary Structure of Laccase Computed Using the VMD Timeline Module[a]

	T	E	B	H	G	I	C
laccase	33.7	36.0	2.4	5.2	2.6	0.0	20.1
laccase + graphene	33.6	34.1	2.0	4.9	3.0	0.0	22.5
laccase + HGr	32.0	36.8	1.8	5.1	2.8	0.0	21.5

[a]The laccase enzyme has been studied in water alone and when it is bound to single layer of graphene and reduced graphene oxide.

The analysis shows that the secondary structure of the laccase enzyme is significantly altered when it is bound to graphene or HGr surfaces. As the catalytic function of the enzyme is dictated by the structure of the enzyme, it can be deduced that the catalytic activity is altered depending upon the surface on which the enzyme is immobilized. Further, quantum chemical calculations using cluster models of enzyme (in water solvent or when it is bound to graphene or HGr) are required to address how much the reaction kinetics is altered by the secondary structural changes of the laccase enzyme.

As represented in Scheme 1, we developed a heteroatom graphene-based bioelectrode for biosensors and bioelectronics applications. Herein, we have started from a novel approach to insert heteroatoms into the pristine graphene layer through a modified single-step CVD method. Also, we utilized the PEDOT:PSS interpolymer complex as the smart interface to easily disperse HGr while combining the system with laccase as the biocatalyst. Figure S1 (Supporting Information) shows the schematic of the CVD setup for the synthesis while the overall equation of the reaction representing the CVD synthesis of HGr is presented in Figure S2 (Supporting Information). The reaction took place at atmospheric pressure and at 850 °C, and the duration of the synthesis reaction was 2 min.

Morphological characterization of the heteroatom graphene was done using TEM and AFM, Raman and XRD spectroscopies were used to determine the atomic electronic features and crystallinity, respectively, and EDS and XPS were used to determine the elemental composition, functional groups, and stoichiometry.

The Raman chart is presented in Figure 1a. Raman spectroscopy is a signature-like characterization technique for the sp^2-hybridized carbon material. The presence of G and D bands is a confirmation of the graphitic nature of the sample under analysis. Two prominent peaks are observed in our sample, as shown in Figure 1a, which corresponds to 1, D-band at 1341 cm^{-1}, and 2, G-band at 1583 cm^{-1}. The G-band is attributed to the stretching of sp^2-hybridized C−C bond, and it is due to the E_{2g} mode.[38,39] The D-band is caused by lattice vacancy and topological defects, and it originates from bonding and antibonding orbitals in the lattice of the graphene plane.[39,40] The presence of the D-band can be attributed to the presence of dopants in the synthesized material.[38]

The XPS analysis of the as-synthesized HGr is presented in Figure 1b(i−iii). The spectrum for the Cl_2p orbital [Figure 1b(i)] is deconvoluted into three peaks at the binding energy (BE) (1) 201.94 eV, (2) 200.24 eV, and (3) 198.43 eV. The peaks at BE 201.94 and 200.24 eV (1 and 2) correspond to covalent C−Cl bonds,[41] the Cl_2p peak at BE 198.43 eV is attributed to Cl^- inorganic chloride;[42] in the present study, this could indicate an edge attached chlorine to which the hydrogen atom is attached. The BE range for the C_1s orbital is presented in Figure 1b(ii), and the spectrum is also deconvoluted into seven peaks [Figure 1b(ii)], (1−7). We notice that peaks 1−6 are reproduced as an inset of the figure to highlight the peaks because their presence is quite significant with respect to the electrocatalytic properties of HGr. The C_1s peak at BE 1 at 290.71 eV is attributed to C═O groups, 2 at 288.93 eV is attributed to C−O groups, 3 at 287.46 eV is attributed to C−O−N groups, 4 at 286.25 eV is attributed to C−Cl groups, 5 at 285.30 eV is attributed to C_1s atoms having sp^3 hybridization, 6 at 283.50 eV is attributed to C−CH_3 groups, and 7 at 284.50 eV is attributed to C_1s atoms having sp^2 hybridization.[43−45] Figure 1b (iii) shows the XPS spectrum for the N_1s orbital BE range, and it is deconvoluted into three peaks; BE 1 at 403.10 eV is attributed to pyrrolic nitrogen; 2 at 400.70 eV is attributed to graphitic or substituted nitrogen, which is an n-type dopant and introduces

Scheme 1. Heteroatom Graphene-Modified Bioelectrode Fabrication Steps

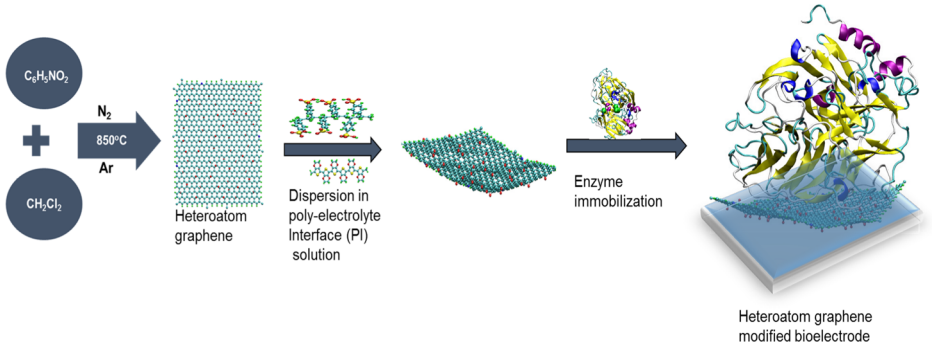

DOI: 10.1021/acsami.9b01914
ACS Appl. Mater. Interfaces 2019, 11, 11238−11250

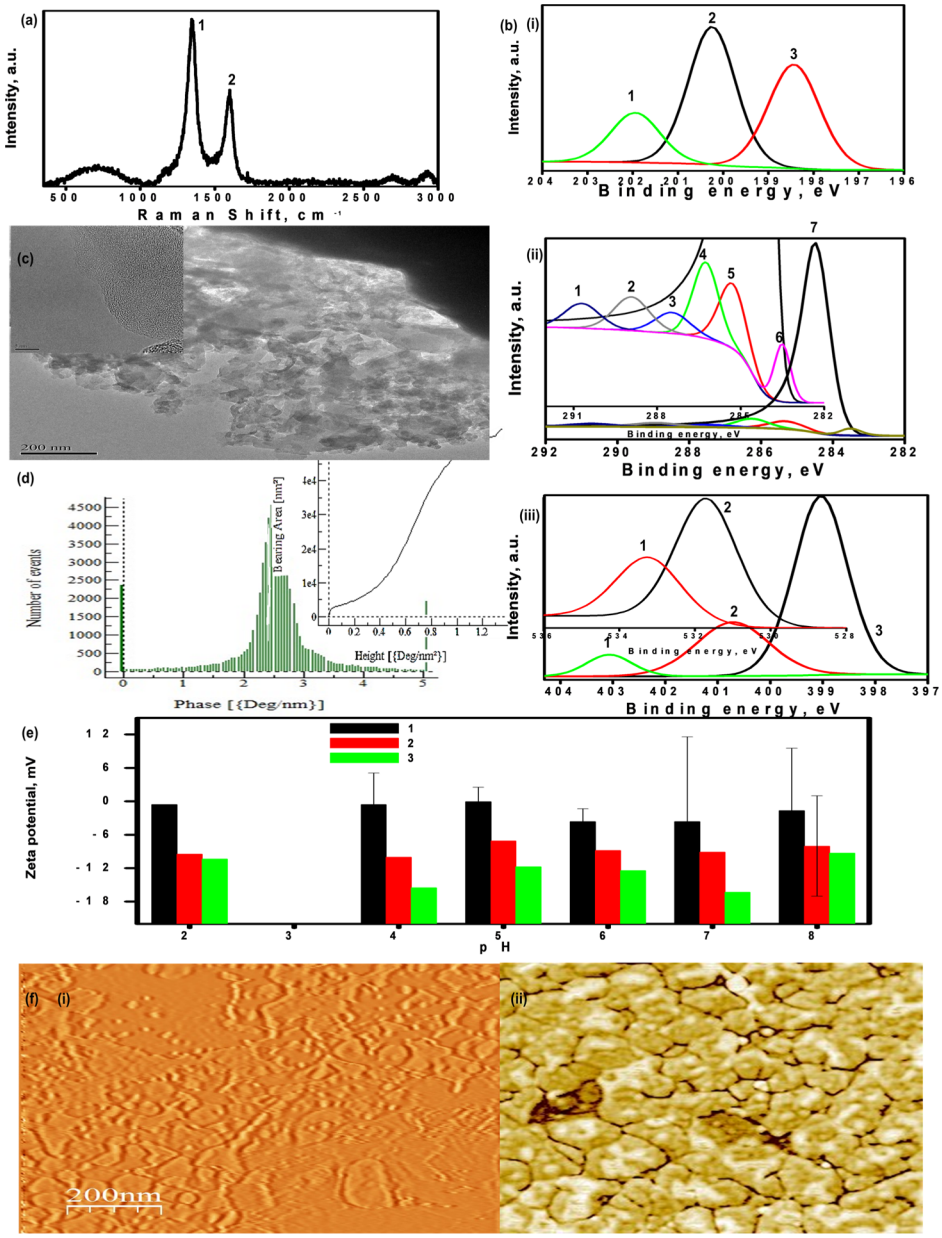

Figure 1. (a) Raman spectrum; (b) XPS spectra for (i) Cl_2p, (ii) C_1s, and (iii) N_1s (with O_1s as inset) BE regions; (c) TEM (inset HRTEM) image; (d) AFM tapping mode phase histogram (inset height profile); (e) zeta potential bar chart; and (f) AFM tapping mode image (i) before and (ii) after enzyme immobilization, for the heteroatom graphene (HGr).

a lone pair of electron into the π system of the graphene and creates an active site for electron transfer on the basal plane at the point of insertion; and 3 at 399.04 eV is attributed to pyridinic nitrogen.[46−48] The XPS spectrum for the O_1s orbital BE range is presented as an inset in Figure 1b(iii); the O_1s peak is deconvoluted into two peaks at BE 1 at 533.24 eV, which is attributed to the C−O group, and 2 at 531.70 eV attributed to the C═O group.[49,50]

The morphological characterization for HGr was performed using TEM and AFM. The TEM result is presented in Figure 1c, and the high-resolution TEM (HRTEM) result is presented as the inset of Figure 1c. The TEM image shows the material as flakelike structures with a thickness of about 2 nm, whereas the HRTEM image shows the as-synthesized material to be highly crystalline in nature with regions of five to seven layers. Figure 1d is the tapping mode AFM histogram showing the average height of HGr to be about 2.5 nm, whereas the inset of Figure 1d shows the maximum height within the area under analysis to be 1.2 nm.

The dispersions of HGr and Gr within the PI solution were evaluated through zeta potential measurements at 25 °C and at different pH values. Zeta potential results supply valuable information about the surface charge of materials in aqueous medium, which is quite valuable for assessing the interactions between solid and liquid phases as well as allowing researchers to have a good understanding of interactions not only at the interface but also during the biocatalytic reaction (Figure 1e). As clearly seen in the figure, the PI−HGr system consistently displays a more electronegative surface charge value for all experiments in the wide pH range of 2−8. This result indicates the presence of negatively charged polar groups distributed

DOI: 10.1021/acsami.9b01914
ACS Appl. Mater. Interfaces 2019, 11, 11238−11250

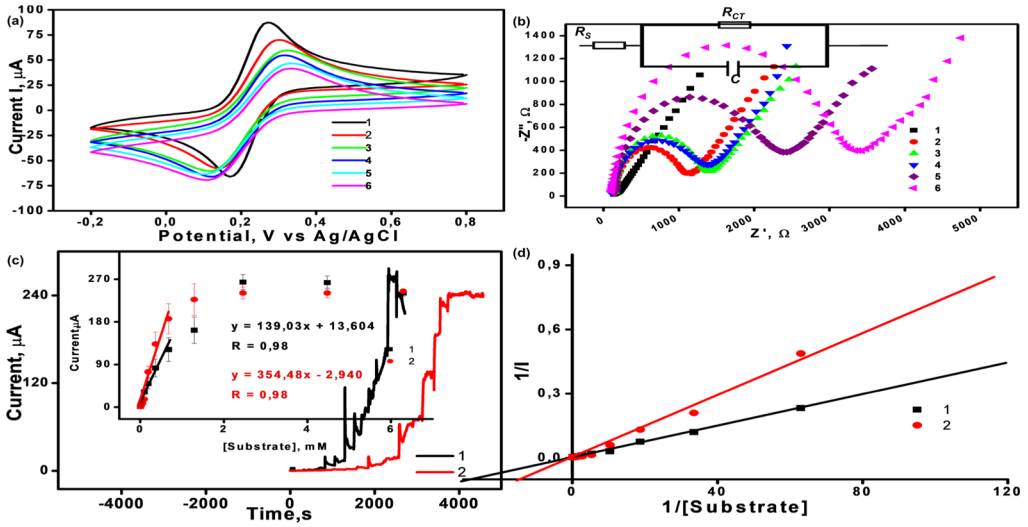

Figure 2. (a) CV and (b) EIS in 10 mM ferrocyanide and 0.1 M KCl solution using 1, bare GC; 2, PI/GC; 3, Gr/PI/GC; 4, HGr/PI/GC; 5, Lac-Gr/PI/GC; and 6, Lac-HGr/PI/GC electrodes. (c) Amperometric response in 0.1 M acetate buffer and 0.1 M KCl solution (inset, calibration plot) using 1, Lac-HGr/PI/GC and 2, Lac-Gr/PI/GC electrodes at a constant applied potential of +0.5 V. (d) Enzyme kinetic modelling plot using the Lineweaver–Burk double reciprocal equation for 1, Lac-HGr/PI/GC and 2, Lac-Gr/PI/GC electrodes.

through the basal plane of our material, as shown by other characterization methods.

AFM at the tapping mode was utilized to observe the height profile and basal plane of the as-synthesized images for HGr and Lac-HGr particles and are presented in Figure 1f(i and ii), respectively. It should be noticed here that the bioelectrode preparation procedure was followed, except a gold substrate was used instead of the GCE. As given in Figure 1d, the thickness of flat materials is about 2.5 nm, which is a confirmation of the TEM characterization. After enzyme incorporation into the biointerface, the appearance of the surface was completely converted into an amorphous and rough structure. The increase in the thickness from 2.5 to 5.0 nm also indicated the high affinity and compatibility between HGr and laccase. This enhances the electrocatalytic activity and electron mobility because of the compact structure created and the proximity of the polar electronegative group with laccase.

EDS and XRD characterizations of the as-synthesized HGr are presented in Figure S3a,b Supporting Information, respectively. EDS is a tool for the analysis of the elemental composition of a sample.[51] The EDS chart shows the presence of carbon, oxygen, copper, aluminum, silicon, and calcium, which revealed the presence of some trace elements.

The presence of copper could be attributed to the copper substrate used as a collector while the presence of aluminum could be attributed to the aluminum stub used for the electron gun. In addition, the presence of silicon may be attributed to the quartz material that was used in the CVD synthesis of HGr, whereas the presence of calcium might have stemmed from handling during sample preparation. Table S1 summarizes the elemental composition of Gr and HGr, as obtained by EDS and XPS analysis, respectively. As given in Figure S3b (Supporting Information), the XRD pattern of the as-synthesised HGr has four peaks at 2θ, (1) 37.8°, (2) 44°, (3) 64.6°, and (4) 77.6°, corresponding to Miller's index values of 021, 101, 203, and 110, respectively. These indices are ascribed to sp^2-hybridized hexagonal carbon peak positions with bond angle 120°.[52]

To evaluate the fabricated electrodes, the electrochemical characterization was also applied through CV and electrochemical impedance spectroscopy (EIS) (Figure 2a,b). It should be noted here that the results are reported in the Supporting Information file in more detail [Figure S4a,b(i–vi)]. The CV and EIS measurements were carried out using 10 mM ferrocyanide solution and 0.1 M phosphate-buffered saline (PBS) solution. CV, in addition to providing information about the reversibility of a redox reaction, could be used to measure the rate constant of an electrochemical reaction using the following equations.

For a typical redox reaction represented by eqs 1 and 2

$$A + e^- \xrightarrow{k_{red}} A_{red} \quad (1)$$

$$A_{red} \xrightarrow{k_{ox}} A + e^- \quad (2)$$

The oxidative and reductive currents (i_A and $i_{A_{red}}$) can be calculated using the following equations

$$i_A = FS_a k_{ox}[A_{red}] \quad (3)$$

$$i_{A_{red}} = -FS_a k_{red}[A] \quad (4)$$

where F is the Faraday constant, S_a is the electrode surface area, k_{ox} is the oxidative rate constant, and k_{red} is the reductive rate constant. Thus, CV is a simple way of evaluating the electrode kinetics, and the peak to peak potential separation (ΔE_p) in CV is also an easy way of determining the electron-transfer kinetics. A narrow ΔE_p indicates fast electron-transfer kinetics, while a wider ΔE_p indicates slower electron-transfer kinetics.[2,53] Figure 2a shows the classical sigmoidal shape with oxidation and reduction peaks observed for all modified electrodes in 10 mM ferrocyanide solution and 0.1 M PBS solution as the supporting electrolytes, which indicated an active electron transfer at the electrode surface–electrolyte solution interface. Moreover, it is observed that the electron-transfer rate kinetics is the fastest in the bare GCE [Figure 2a(1)] and the slowest in Lac-Gr/PI/GCE (Figure 2a(6)). It is however observed that the HGr-modified electrode systems

DOI: 10.1021/acsami.9b01914
ACS Appl. Mater. Interfaces 2019, 11, 11238–11250

consistently exhibit a narrower ΔE_p in comparison to Gr-modified electrode systems, which could probably be attributed to the presence of heteroatoms in the lattice of HGr. The effect of scan rates (10 mV/s) for the bare GCE and the modified electrodes on the cathodic peak currents I_{pc} and the anodic peak currents I_{pa} are presented in Figure S4(i–vii) (Supporting Information). I_{pc} and I_{pa} were observed to increase linearly with increasing scan rates, which indicated the diffusion-controlled electrode process.[54,55]

The impedance plots for the bare GCE and the modified electrodes are presented in Figure 2b, whereas the circuit equivalent diagram for the electrochemical system is given as the inset. Two regions are observed in the plots for all electrodes, namely the kinetic control region (the semicircles) and the mass transfer or diffusion-controlled region (the linear lines). The kinetic control impedance is influenced by the reaction kinetics on the surface of the electrode, thus slower kinetics results in larger semicircle portion of the plot; equally, the diffusion control impedance is influenced by the concentration of the ionic species in the electrolyte, and a higher concentration will result in a low mass-transfer (or diffusion-controlled) resistance. It is observed that the kinetic control region for the bare GCE [Figure 2b(1)] is quite negligible when compared to those of the modified electrodes. The result signified a very low resistance for the kinetics-controlled process on the surface of the bare electrode. It is observed that there is increasing kinetic control resistance from plots (2)–(6) representing 2 PI-modified electrode, 3 Gr-modified electrode, 4 HGr-modified electrode, 5 Lac-Gr-modified electrode, and 6 Lac-HGr-modified electrode. It is also quite interesting to note that the HGr-based modified electrodes [plots (4) and (6)] exhibited higher kinetic controlled impedance than their Gr-based modified electrode counterparts. This could be attributed to the presence of the electronegative species within the HGr graphitic plane, which would repel the electronegative ion of the electrolyte solution.[15,54,56,57]

To show electrobiocatalytic activity of the electrodes, the electrobiocatalytic conversion of hydroquinone to benzophenone in an anaerobic environment using Lac-HGr/PI/GC and Lac-Gr/PI/GC electrodes were monitored by chronoamperometric measurements [Figure 2c(1–2)], whereas the inset is the calibration curve for the respective amperometric response. The amperometric measurements were carried out by using freshly deoxygenated acetate buffer (0.1 M, pH: 5.0) and 0.1 M KCl solution at a constant potential of +0.5 V using Lac-HGr/PI/GC (1) and Lac-Gr/PI/GC (2) electrodes, respectively. The acetate buffer solution was deoxygenated by bubbling nitrogen gas through it for 1 h prior to each measurement.

The electrobiocatalytic conversion of hydroquinone to benzophenone under aerobic conditions was also carried out using the same procedure by skipping nitrogen purge to remove dissolved oxygen from the solution (Figure S5a, Supporting Information). It is observed that the amperometric response of the HGr-modified electrodes in all experiments always reached a steady current within a few seconds, thus indicating faster reaction kinetics. Meanwhile, the response of the Gr-based modified electrodes was much slower, taking up to several minutes before achieving a steady current. It is also observed that, in all experiments, the HGr-modified electrodes generated higher capacitive currents than the corresponding Gr-modified electrodes. Using the Lineweaver–Burk plot, the apparent Michaelis–Menten constant (K_M^{app}) was calculated according to the following double reciprocal equation

$$\frac{1}{I} = \frac{1}{I_{max}} + \frac{K_M^{app}}{I_{max}C} \quad (5)$$

where I is the steady state current after the addition of the substrate, I_{max} is the maximum current reached at the saturation of the substrate, C is the substrate concentration, and K_M^{app} is an indication of the enzyme affinity to the substrate.[56,58] In all experiments, a higher enzyme affinity (K_M^{app}) was achieved with the HGr-modified electrode compared to the corresponding Gr-modified electrodes.

These results emphasized the fact that the presence of heteroatoms in the lattice of graphene facilitated the electrocatalytic reaction at the electrode surface/electrolyte interface, thereby resulting in shorter response time, higher current generation, and, of course, higher enzyme affinity for the substrate. Scheme 1 shows the representation of the bioelectrode fabrication steps, while Schemes 2 and 3 show the electrobiocatalytic sensing of hydroquinone under anaerobic and aerobic conditions, respectively, using laccase-heteroatom graphene-modified bioelectrodes.

Scheme 2. Electrobiocatalytic Sensing of Hydroquinone Using Heteroatom Graphene Modified Bioelectrode in Anaerobic Condition

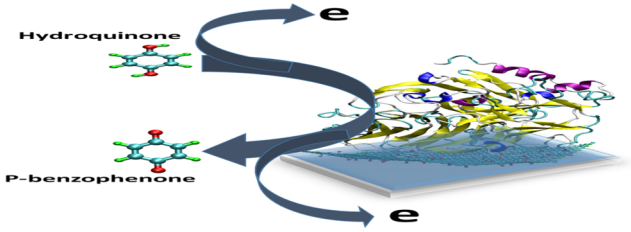

Scheme 3. Electrobiocatalytic Sensing of Hydroquinone Using Heteroatom Graphene-Modified Bioelectrode in Aerobic Condition

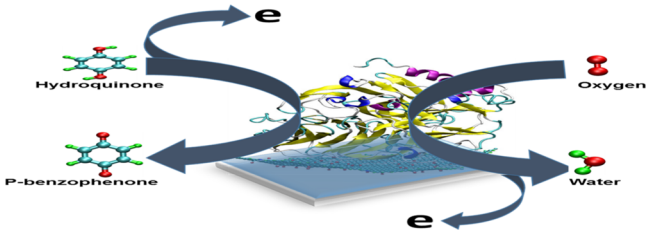

The summary of the sensitivity, linear range, dynamic range, and the enzyme affinity is presented in Table 3. The electrocatalysis reaction experiments were again carried out using hydroquinone as a sample substrate, and the electrode modifications were done exactly as in previous experiments but this time without immobilization of an enzyme.

The amperometric response with the calibration curves as the inset is presented in Figure S6 (a) (for anaerobic electrocatalysis) and (b) (for aerobic electrocatalysis) of the Supporting Information; it is again observed that the amperometric response and reaction kinetics are faster when HGr-modified electrodes are used than when Gr-modified electrodes are used. The corresponding reaction kinetics modelling plot using the double reciprocal equation is also

DOI: 10.1021/acsami.9b01914
ACS Appl. Mater. Interfaces 2019, 11, 11238–11250

Table 3. Summary of the Results of the Amperometric Response for the Electrocatalytic Oxidation of Hydroquinone

electrode	sensitivity μA/mM/cm^2	dynamic range (mM)	linear range (mM)	apparent Michaelis Menten constant K_M^{app}
Lac-HGr/PI/GC (anaerobic)	1986.14	0.01−2.42	0.01−1.24	0.9
Lac-Gr/PI/GC (anaerobic)	5064.00	0.07−1.28	0.07−0.65	0.39
Lac-HGr/PI/GC (aerobic)	1214.29	0.03−11.00	0.03−2.30	1.58
Lac-Gr/PI/GC (aerobic)	602.86	0.04−7.68	0.04−2.47	1.44

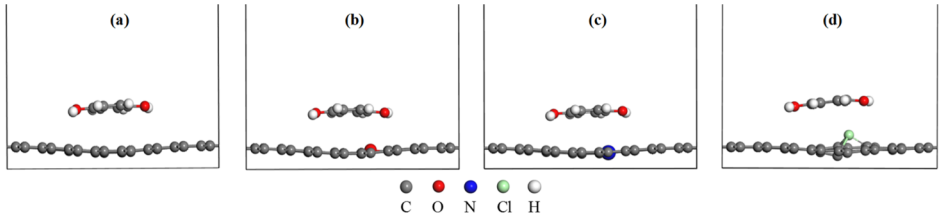

Figure 3. Favorite adsorption configurations of hydroquinone molecule adsorbed onto the (a) pristine, (b) O-, (c) N-, and (d) Cl-doped graphene nanosheets.

Table 4. Results of Favorite Adsorption Energies (E_{ads}), Adsorption Distance (d), Charge Transfer (Δq), and Work Function (Φ) of Hydroquinone and *p*-Benzophenone Molecules Adsorption onto the Surface of Graphene Nanosheets with or without O-, N-, and Cl-Dopants

molecules	systems	E_{ads} (eV)	d (Å)	Δq lel	Φ (eV)
hydroquinone	pristine graphene	−0.54	3.98	−0.06	4.31
	O-doped graphene	−0.66	2.95	−0.09	3.99
	N-doped graphene	−0.88	2.97	−0.23	3.66
	Cl-doped graphene	−0.91	2.64	−0.25	3.51
p-benzophenone	pristine graphene	−0.89	3.04	−0.20	4.11
	O-doped graphene	−1.13	2.82	−0.26	3.78
	N-doped graphene	−1.59	2.61	−0.29	3.61
	Cl-doped graphene	−2.25	2.28	−0.34	3.24

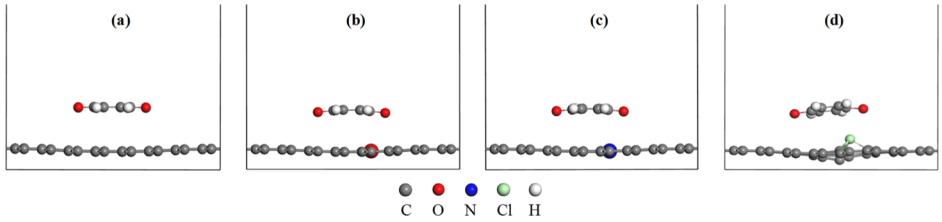

Figure 4. Favorite adsorption configurations of *p*-benzophenone molecule adsorbed onto the surface of (a) pristine, (b) O-, (c) N-, and (d) Cl-doped graphene nanosheets.

presented in Figure S6c,d. Detailed characterization of Gr has been published in our previous work DOI: 10.1016/j.bios.2016.03.063. These reactions confirm the electrocatalytic properties of graphene and heteroatom graphene.[59−63]

Adsorption of Hydroquinone Molecule on Pristine, O-, N-, and Cl-Doped Graphene. The adsorption property of hydroquinone molecule onto O-, N-, and Cl-doped graphene was initially considered, as indicated in Figure 3.

The corresponding adsorption energy, adsorption distance, work function, and charge transfer of hydroquinone and *p*-benzophenone molecules on the O-, N-, and Cl-doped graphene nanosheet surfaces are summarized in Table 4.

The bond lengths between the O (1.50, 1.49, and 1.47 Å), N (1.45, 1.45, and 1.45 Å) and Cl (1.74, 2.37, and 1.72 Å) atoms and each neighboring C atom were considerable larger than that of the C−C bonds in pristine graphene nanosheets (1.42, 1.42, and 1.43 Å). The protrusion of the O, N, and Cl atoms on the surface of graphene nanosheets was due to the larger atomic radius of the O, N, and Cl atoms compared with that of the C atom.[64−66] This protrusion can reduce the steric effect in the adsorption process and may induce higher adsorption energy compared to pristine graphene nanosheets. The elongated bond length forces the O, N, and Cl atoms to protrude from the graphene sheets, also making the positions of the neighboring O, N, and Cl atoms out of plane. The hydroquinone molecule was found to bind to O-, N-, and Cl-doped graphene nanosheets with relatively weak adsorption energies of −0.66, −0.88, and −0.91 eV, respectively, which were higher than that of the pristine graphene nanosheets (−0.54 eV). The adsorption of hydroquinone molecule onto the pristine graphene nanosheets was in a typical physisorption state based on the adsorption energy <0.5 eV, whereas the adsorption onto O-, N-, and Cl-doped graphene nanosheet surfaces was weak chemisorption. The adsorption distances between O, N, and Cl dopants and the C atom in the hydroquinone molecule were 3.98, 2.95, 2.97, and 2.64 Å for the pristine, O-, N-, and Cl-doped graphene nanosheets, respectively, which signified a relatively weak covalent bond between the O, N, and Cl dopants and the C atom in the hydroquinone molecule. The theoretical studies showed that

DOI: 10.1021/acsami.9b01914
ACS Appl. Mater. Interfaces 2019, 11, 11238−11250

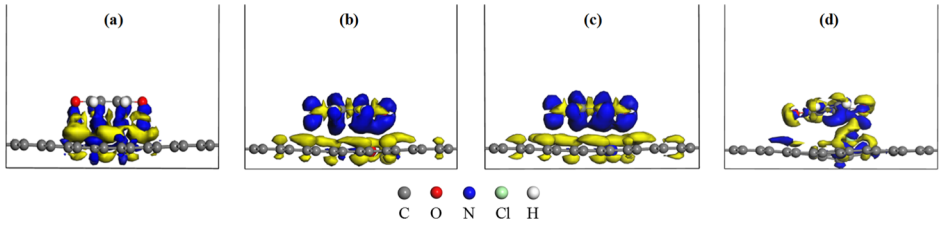

Figure 5. CDDs upon hydroquinone molecule adsorption onto pristine, O-, N-, and Cl-doped graphene nanosheet surfaces showing regions of charge depletion (yellow) and accumulation (blue) with an isovalue of 0.005 e Å^{-3}.

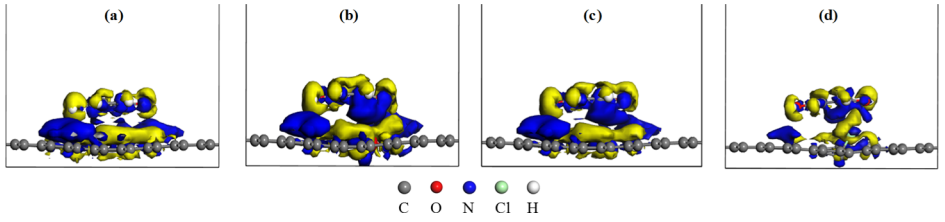

Figure 6. CDDs upon *p*-benzophenone molecule adsorption onto pristine, O-, N-, and Cl-doped graphene nanosheet surfaces showing regions of charge depletion (yellow) and accumulation (blue) with an isovalue of 0.005 e Å^{-3}.

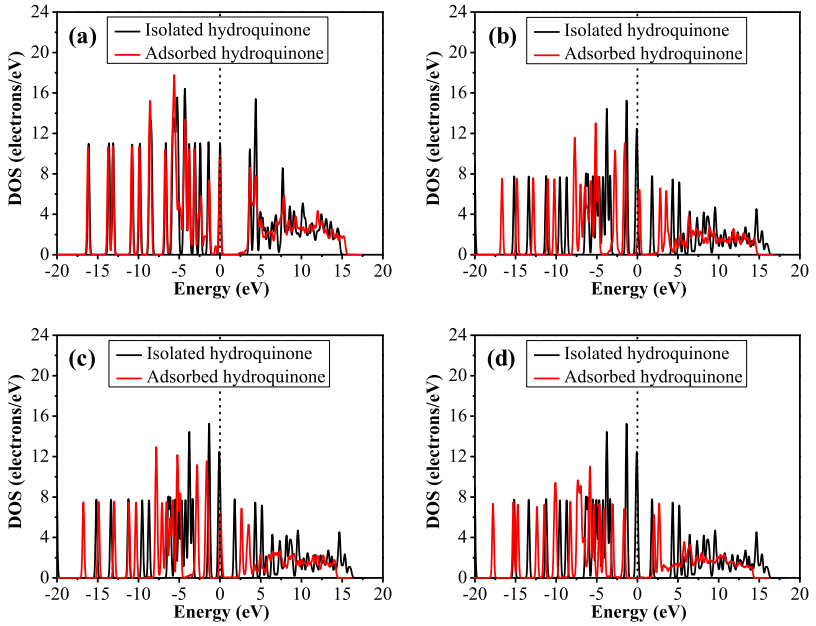

Figure 7. DOS of hydroquinone molecule before and after adsorption on the (a) pristine, (b) O-, (c) N-, and (d) Cl-doped graphene nanosheet surfaces. The Fermi energy level is shown as a dashed vertical line.

the adsorption of hydroquinone molecule on Cl-doped graphene nanosheet surfaces was the strongest (i.e., stronger sensing capability) among the O- and N-doped graphene nanosheet systems. Therefore, by considering these results, Cl doping was found to be an efficient approach to fully enhance the adsorption ability of pristine graphene nanosheets.

Adsorption of *p*-Benzophenone Molecule on Pristine, O-, N-, and Cl-Doped Graphene. The adsorption of *p*-benzophenone molecule adsorbed onto the pristine, O-, N-, and Cl-doped graphene nanosheets was further investigated. After geometry optimization, the most favorable adsorption configurations were obtained, as given in Figure 4, and the corresponding adsorption energy and structure parameters are also presented in Table 4.

As given in Table 4, the adsorption energies of *p*-benzophenone molecule adsorbed onto the surface of O-, N-, and Cl-doped graphene nanosheets were obtained as −1.13, −1.59, and −2.25 eV, respectively, which were much stronger than that on pristine graphene nanosheets (−0.89 eV). Therefore, after O-, N-, and Cl-dopings, the adsorption of *p*-benzophenone molecule onto graphene nanosheets can be greatly enhanced, that is, the O-, N-, and Cl-doped graphene nanosheets would be a promising material for *p*-benzophenone removal. The adsorption energies of *p*-benzophenone molecule onto O-, N-, and Cl-doped graphene nanosheet surfaces revealed that all binding reactions occurred through an exothermic process in the range of chemical adsorption, which is also confirmed by the short adsorption distance (2.82, 2.61, and 2.28 Å for O-, N-, and Cl-doped graphene nanosheets, respectively, see Table 4). When considering the interactions between the O-, N-, and Cl-dopants and the *p*-benzophenone molecule, the Cl dopant interaction with the *p*-

DOI: 10.1021/acsami.9b01914
ACS Appl. Mater. Interfaces 2019, 11, 11238−11250

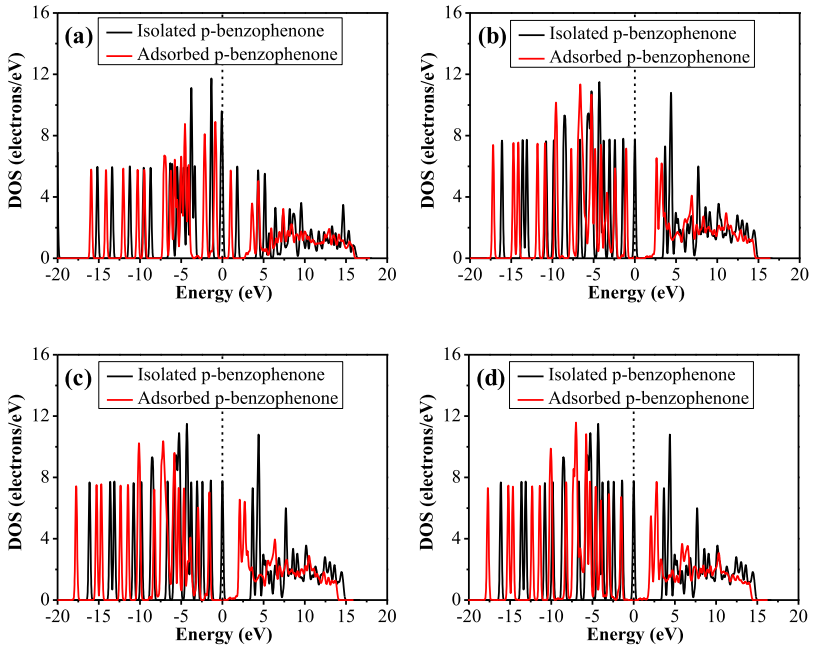

Figure 8. DOS of *p*-benzophenone molecule before and after adsorption onto the (a) pristine, (b) O-, (c) N-, and (d) Cl-doped graphene nanosheet surfaces. The Fermi energy level is shown as a dashed vertical line.

benzophenone molecule was remarkably much larger than that of the O and N dopants. This revealed that the Cl-doped graphene nanosheets exhibited the strongest binding interactions and sensitivity with *p*-benzophenone molecule to form a stable complex. This may be due to the strengths of the valence electrons affecting the chemical properties. Compared with earlier reports, the Cl-doped graphene nanosheets showed much better adsorption performance than the cellulosic $(1\bar{1}0)$ and (200) surfaces for benzophenone adsorption[67] and hydroquinone adsorption on C_{60} fullerene[68] and the Al- and Si-doped boron nitride nanotubes.[69]

Charge Transfer and DOS. The electron density distribution of hydroquinone and *p*-benzophenone molecules adsorbed on the pristine, O-, N-, and Cl-doped graphene nanosheets were based on the CDD and Hirshfeld charge analysis. The CDD plot of hydroquinone and *p*-benzophenone molecules adsorption on the pristine, O-, N-, and Cl-doped graphene nanosheets is shown in Figures 5 and 6.

It is clearly shown that a large electron density depletion (yellow region) appears in the area around the adsorbed molecules and above the Cl atom. This revealed that the doped Cl atom served as a bridge to connect the electron clouds of the graphene nanosheets and the adsorbed molecules. Thus, the interactions of electrons were much stronger, inducing much stronger adsorption energy of hydroquinone and *p*-benzophenone molecules onto Cl-doped graphene nanosheets, which agreed well with the above adsorption results. Moreover, an electron density accumulation (blue region) is seen around the surface of graphene nanosheets. By analysing the DOS of the most favorable configuration, further insight into the bonding mechanism can be obtained. As shown in Figures 7 and 8, the DOS of hydroquinone and *p*-benzophenone molecules were obviously changed near the Fermi energy level after adsorption, revealing that hydroquinone and *p*-benzophenone molecules have an intense reaction with the O-, N-, and Cl-doped graphene nanosheet surfaces.

The Hirshfeld charge analysis was also used to calculate the charge transfer for the adsorption of hydroquinone and *p*-benzophenone molecules onto the pristine, O-, N-, and Cl-doped graphene nanosheet surfaces. The Hirshfeld charge analysis indicated that −0.06, −0.09, −0.23, and −0.25 |e| (see Table 4) transfers from the hydroquinone molecule to the pristine, O-, N-, and Cl-doped graphene nanosheets, respectively. However, *p*-benzophenone molecule adsorption offered a substantial charge transfer of about −0.20, −0.26, −0.29, and −0.34 |e| (see Table 4) from the pristine, O-, N-, and Cl-doped graphene nanosheets, respectively, to the *p*-benzophenone molecule surface, suggesting that *p*-benzophenone molecule served as an electron acceptor. This may induce changes in the conductivity of the pristine and doped graphene nanosheet systems, which might be an efficient property to assist in the design of graphene-based sensors for hydroquinone and *p*-benzophenone molecules removal. The electron transfer between the adsorbed molecules and graphene nanosheets was much stronger after Cl doping, which further confirmed the strong interactions between the adsorbed molecules and the Cl-doped graphene nanosheets.

The changes in the work function, which is related to the charge transfer,[70] were used to evaluate the sensitivity of O-, N-, and Cl-doped graphene nanosheets toward hydroquinone and *p*-benzophenone molecules adsorption. As shown in Table 4, the work function of pristine graphene nanosheets was reduced after hydroquinone and *p*-benzophenone molecules adsorption because of the charge transfer from the O-, N-, and Cl-doped graphene nanosheets to the hydroquinone and *p*-benzophenone molecule surfaces.

CONCLUSIONS

Through careful and painstaking nanoarchitecture, we have developed a highly sensitive and ultrafast bioelectrocatalytic nanostructure for applications in the fabrication of highly efficient, fast, and highly sensitive thin nanosized reactors, biodevices, and energy-storage devices. This has therefore

DOI: 10.1021/acsami.9b01914
ACS Appl. Mater. Interfaces 2019, 11, 11238−11250

paved the way for bulk commercial synthesis of a high quality, cheap, and highly electrocatalytic platform for the fabrication of thin, flexible, sensitive, and superfast bioreactors, bioelectronics, and electrocatalytic devices. The adsorption of hydroquinone and *p*-benzophenone molecules onto the pristine, O-, N-, and Cl-doped graphene nanosheet surfaces was further studied using DFT calculations. We found that after O-, N-, and Cl-dopings, adsorptions of both hydroquinone and *p*-benzophenone molecules were much improved and there was strong chemical adsorption, especially for the *p*-benzophenone adsorption complexes. Moreover, the adsorption improvement mechanism was explored by analyzing the electron density distribution, DOS, and charge transfer, where the doped Cl atom can serve as a bridge to connect the hydroquinone and *p*-benzophenone molecules with graphene nanosheets. Therefore, Cl-doped graphene nanosheets were observed as the most promising adsorbent for hydroquinone and *p*-benzophenone removal. Our experimental study and theoretical calculation offer a primary understanding into O-, N-, and Cl-doping effect on the electronic, adsorption, and structural properties of graphene nanosheets and shed more insights into the application of graphene nanosheets in sensing hydroquinone and *p*-benzophenone molecules.

■ ASSOCIATED CONTENT

Supporting Information

The Supporting Information is available free of charge on the ACS Publications website at DOI: 10.1021/acsami.9b01914.

CVD schematics for the synthesis of heteroatom graphene, overall synthesis equation for the CVD synthesis of heteroatom graphene, EDS and XRD charts for the as-synthesized HGr, CV measurements at scan rates of 10−200 mV/s versus Ag/AgCl in 10 mM ferrocyanide and 0.1 M KCl using bare GC, PI/GC, Gr/PI/GC, HGr/PI/GC, Lac-Gr/PI/GC, and Lac-HGr/PI/GC electrodes and the respective calibration plots, amperometric response to the electrocatalytic conversion of hydroquinone in 0.1 M acetate buffer pH 5 and 0.1 M KCl solution under anaerobic and aerobic conditions, respectively, using HGr/PI/GC and Gr/PI/GC electrodes and the respective calibration curves, and affinity modelling of the electrocatalysis reactions using the Line Weaver Burke double reciprocal plot (PDF)

■ AUTHOR INFORMATION

Corresponding Authors

*E-mail: ezekield@vut.ac.za (E.D.D.).
*E-mail: pennyg@uj.ac.za (P.P.G.).

ORCID

Penny Poomani Govender: 0000-0002-3011-6675

Notes

The authors declare no competing financial interest.

■ ACKNOWLEDGMENTS

The authors would like to acknowledge the financial contributions from the Faculty of Science, Centre for Nanomaterials and Science Research, Department of Applied Chemistry (University of Johannesburg, South Africa), the Research Directorate of Vaal University of Technology, Vanderbijlpark, South Africa, and the National Research Foundation, South Africa (TTK14052167682). The authors are also grateful to the Centre for High Performance Computing (CHPC), Cape Town for the computational resources provided.

■ REFERENCES

(1) Parlak, O.; Tiwari, A.; Turner, A. P. F.; Tiwari, A. Template-Directed Hierarchical Self-Assembly of Graphene Based Hybrid Structure for Electrochemical Biosensing. *Biosens. Bioelectron.* **2013**, *49*, 53−62.

(2) Turner, A. P. *Biosensors: Fundamentals and Applications*; Oxford University Press: New York, 1987.

(3) Patra, S.; Roy, E.; Tiwari, A.; Madhuri, R.; Sharma, P. K. 2-Dimensional Graphene as a Route for Emergence of Additional Dimension Nanomaterials. *Biosens. Bioelectron.* **2017**, *89*, 8−27.

(4) Yola, M. L.; Eren, T.; Atar, N. A novel and sensitive electrochemical DNA biosensor based on Fe@Au nanoparticles decorated graphene oxide. *Electrochim. Acta* **2014**, *125*, 38−47.

(5) Khodadadi, A.; Faghih-Mirzaei, E.; Karimi-Maleh, H.; Abbaspourrad, A.; Agarwal, S.; Gupta, V. K. A New Epirubicin Biosensor Based on Amplifying DNA Interactions with Polypyrrole and Nitrogen-Doped Reduced Graphene: Experimental and Docking Theoretical Investigations. *Sens. Actuators, B* **2019**, *284*, 568−574.

(6) Yola, M. L.; Atar, N.; Üstündağ, Z.; Solak, A. O. A Novel Voltammetric Sensor Based on P-Aminothiophenol Functionalized Graphene Oxide/Gold Nanoparticles for Determining Quercetin in the Presence of Ascorbic acid. *J. Electroanal. Chem.* **2013**, *698*, 9−16.

(7) Gupta, V. K.; Atar, N.; Yola, M. L.; Üstündağ, Z.; Uzun, L. A novel magnetic Fe@Au core-shell nanoparticles anchored graphene oxide recyclable nanocatalyst for the reduction of nitrophenol compounds. *Water Res.* **2014**, *48*, 210−217.

(8) Yola, M. L.; Eren, T.; Atar, N. A Sensitive Molecular Imprinted Electrochemical Sensor Based on Gold Nanoparticles Decorated Graphene Oxide: Application to Selective Determination of Tyrosine in Milk. *Sens. Actuators, B* **2015**, *210*, 149−157.

(9) Gupta, V. K.; Yola, M. L.; Qureshi, M. S.; Solak, A. O.; Atar, N.; Üstündağ, Z. A Novel Impedimetric Biosensor Based on Graphene Oxide/Gold Nanoplatform for Detection of DNA arrays. *Sens. Actuators, B* **2013**, *188*, 1201−1211.

(10) Yola, M. L.; Eren, T.; Atar, N.; Saral, H.; Ermiş, İ. Direct-methanol Fuel Cell Based on Functionalized Graphene Oxide with Mono-metallic and Bi-metallic Nanoparticles: Electrochemical Performances of Nanomaterials for Methanol Oxidation. *Electroanalysis* **2015**, *28*, 570−579.

(11) Atar, N.; Eren, T.; Yola, M. L.; Karimi-Maleh, H.; Demirdögen, B. Magnetic Iron Oxide and Iron Oxide@Gold Nanoparticle Anchored Nitrogen and Sulfur-Functionalized Reduced Graphene Oxide Electrocatalyst for Methanol Oxidation. *RSC Adv.* **2015**, *5*, 26402−26409.

(12) Liu, J.; Liu, Z.; Barrow, C. J.; Yang, W. Molecularly Engineered Graphene Surfaces for Sensing Applications: A review. *Anal. Chim. Acta* **2015**, *859*, 1−19.

(13) Turner, A. P. F. Biosensors: Sense and Sensibility. *Chem. Soc. Rev.* **2013**, *42*, 3184−3196.

(14) Tiwari, A.; Nordin, A. N. *Advanced Biomaterials and Biodevices*; John Wiley & Sons, 2014.

(15) Kuila, T.; Bose, S.; Khanra, P.; Mishra, A. K.; Kim, N. H.; Lee, J. H. Recent advances in graphene-based biosensors. *Biosens. Bioelectron.* **2011**, *26*, 4637−4648.

(16) Sharon, M.; Sharon, M.; Shinohara, H.; Tiwari, A. *Graphene: An Introduction to the Fundamentals and Industrial Applications*; Wiley, 2015.

(17) Guo, B.; Fang, L.; Zhang, B.; Gong, J. R. Graphene Doping: A Review. *Insci. J.* **2011**, *1*, 80−89.

(18) Sheng, Z.-H.; Zheng, X.-Q.; Xu, J.-Y.; Bao, W.-J.; Wang, F.-B.; Xia, X.-H. Electrochemical Sensor Based on Nitrogen Doped Graphene: Simultaneous Determination of Ascorbic Acid, Dopamine and Uric Acid. *Biosens. Bioelectron.* **2012**, *34*, 125−131.

DOI: 10.1021/acsami.9b01914
ACS Appl. Mater. Interfaces 2019, 11, 11238−11250

(19) Wang, L.; Ambrosi, A.; Pumera, M. "Metal-Free" Catalytic Oxygen Reduction Reaction on Heteroatom-Doped Graphene is Caused by Trace Metal Impurities. *Angew. Chem., Int. Ed. Engl.* **2013**, *52*, 13818−13821.
(20) Parlak, C.; Alver, Ö. A Density Functional Theory Investigation on Amantadine Drug Interaction with Pristine and B, Al, Si, Ga, Ge Doped C60 Fullerenes. *Chem. Phys. Lett.* **2017**, *678*, 85−90.
(21) Safari, M.; Ghiaci, M.; Jafari-Asl, M.; Ensafi, A. A. Nanohybrid Organic−Inorganic Chitosan/Dopamine/Tio2 Composites with Controlled Drug-Delivery Properties. *Appl. Surf. Sci.* **2015**, *342*, 26−33.
(22) Bertrand, T.; Jolivalt, C.; Briozzo, P.; Caminade, E.; Joly, N.; Madzak, C.; Mougin, C. Crystal Structure of a Four-Copper Laccase Complexed with an Arylamine: Insights into Substrate Recognition and Correlation with Kinetics. *Biochemistry* **2002**, *41*, 7325−7333.
(23) Poole, P. H.; Sciortino, F.; Essmann, U.; Stanley, H. E. Phase behaviour of metastable water. *Nature* **1992**, *360*, 324−328.
(24) Wang, J.; Wolf, R. M.; Caldwell, J. W.; Kollman, P. A.; Case, D. A. Development and Testing of a General Amber Force Field. *J. Comput. Chem.* **2004**, *25*, 1157−1174.
(25) Case, D.; Darden, T.; Cheatham, T., III; Simmerling, C.; Wang, J.; Duke, R.; Luo, R.; Walker, R.; Zhang, W.; Merz, K. *AMBER 12*; University of California: San Francisco, 2012; pp 1−826.
(26) Segall, M. D.; Lindan, P. J. D.; Probert, M. J.; Pickard, C. J.; Hasnip, P. J.; Clark, S. J.; Payne, M. C. First-Principles Simulation: Ideas, Illustrations and the CASTEP Code. *J. Phys.: Condens. Matter* **2002**, *14*, 2717−2744.
(27) *Materials Studio Simulation Environment*. Release 2016; Accelrys Software Inc: San Diego, CA, 2016.
(28) Perdew, J. P.; Burke, K.; Ernzerhof, M. Generalized Gradient Approximation made Simple. *Phys. Rev. Lett.* **1996**, *77*, 3865−3868.
(29) Sun, B.-Z.; Chen, W.-K.; Wang, X.; Lu, C.-H. A Density Functional Theory Study on the Adsorption and Dissociation of N_2O on Cu_2O (111) Surface. *Appl. Surf. Sci.* **2007**, *253*, 7501−7505.
(30) Chen, W.-K.; Cao, M.-J.; Liu, S.-H.; Lu, C.-H.; Xu, Y.; Li, J.-Q. A first-principles study of the chemi-adsorption of benzene on Au(100) surface. *Chem. Phys. Lett.* **2006**, *417*, 414−418.
(31) Vanderbilt, D. Soft Self-Consistent Pseudopotentials in a Generalized Eigenvalue Formalism. *Phys. Rev. B: Condens. Matter Mater. Phys.* **1990**, *41*, 7892−7895.
(32) Tkatchenko, A.; Scheffler, M. Accurate Molecular Van Der Waals Interactions from Ground-State Electron Density and Free-Atom Reference Data. *Phys. Rev. Lett.* **2009**, *102*, 073005.
(33) Monkhorst, H. J.; Pack, J. D. Special Points for Brillouin-Zone Integrations. *Phys. Rev. B: Solid State* **1976**, *13*, 5188−5192.
(34) Billeter, S. R.; Turner, A. J.; Thiel, W. Linear Scaling Geometry Optimisation and Transition State Search in Hybrid Delocalised Internal Coordinates. *Phys. Chem. Chem. Phys.* **2000**, *2*, 2177−2186.
(35) Hirshfeld, F. L. Bonded-Atom Fragments for Describing Molecular Charge Densities. *Theor. Chim. Acta* **1977**, *44*, 129−138.
(36) Jorgensen, W. L.; Chandrasekhar, J.; Madura, J. D.; Impey, R. W.; Klein, M. L. Comparison of Simple Potential Functions for Simulating Liquid Water. *J. Chem. Phys.* **1983**, *79*, 926.
(37) Humphrey, W.; Dalke, A.; Schulten, K. VMD: visual molecular dynamics. *J. Mol. Graph.* **1996**, *14*, 33−38.
(38) Matz, D. L.; Sojoudi, H.; Graham, S.; Pemberton, J. E. Signature Vibrational Bands for Defects in CVD Single-Layer Graphene by Surface-Enhanced Raman Spectroscopy. *J. Phys. Chem. Lett.* **2015**, *6*, 964−969.
(39) Ferrari, A. C. Raman spectroscopy of graphene and graphite: Disorder, electron-phonon coupling, doping and nonadiabatic effects. *Solid State Commun.* **2007**, *143*, 47−57.
(40) Sasaki, K.-i.; Tokura, Y.; Sogawa, T. The Origin of Raman D Band: Bonding and Antibonding Orbitals in Graphene. *Crystals* **2013**, *3*, 120−140.
(41) Fedoseeva, Y. V.; Bulusheva, L. G.; Okotrub, A. V.; Asanov, I. P.; Troyanov, S. I.; Vyalikh, D. V. Electronic Structure of the Chlorinated Fullerene $C_{60}Cl_{30}$ Studied by Quantum Chemical Modeling of X-ray Absorption Spectra. *Int. J. Quantum Chem.* **2010**, *111*, 2688−2695.
(42) Mallinson, C. F.; Kozlowski, S.; Harvey, A.; Watts, J. F. An Investigation of the Effect of Chlorinated Solvents on Surface Characteristics of S-65 Beryllium. *Surf. Interface Anal.* **2016**, *48*, 689−693.
(43) Yu, X.; Xu, P.; Hua, T.; Han, A.; Liu, X.; Wu, H.; Du, P. Multi-Walled Carbon Nanotubes Supported Porous Nickel Oxide as Noble Metal-Free Electrocatalysts for Efficient Water Oxidation. *Int. J. Hydrogen Energy* **2014**, *39*, 10467−10475.
(44) Corcoran, C. J.; Tavassol, H.; Rigsby, M. A.; Bagus, P. S.; Wieckowski, A. Application of XPS to Study Electrocatalysts for Fuel Cells. *J. Power Sources* **2010**, *195*, 7856−7879.
(45) de Souza, J. C. P.; Iost, R. M.; Crespilho, F. N. Nitrated Carbon Nanoblisters for High-Performance Glucose Dehydrogenase Bioanodes. *Biosens. Bioelectron.* **2016**, *77*, 860−865.
(46) Hwang, J. O.; Park, J. S.; Choi, D. S.; Kim, J. Y.; Lee, S. H.; Lee, K. E.; Kim, Y.-H.; Song, M. H.; Yoo, S.; Kim, S. O. Workfunction-Tunable, N-Doped Reduced Graphene Transparent Electrodes for High-Performance Polymer Light-Emitting Diodes. *ACS Nano* **2011**, *6*, 159−167.
(47) Yang, W.; Xu, X.; Tu, Z.; Li, Z.; You, B.; Li, Y.; Raj, S. I.; Yang, F.; Zhang, L.; Chen, S.; Wang, A. Nitrogen Plasma Modified CVD Grown Graphene as Counter Electrodes for Bifacial Dye-Sensitized Solar Cells. *Electrochim. Acta* **2015**, *173*, 715−720.
(48) Blume, R.; Rosenthal, D.; Tessonnier, J.-P.; Li, H.; Knop-Gericke, A.; Schlögl, R. Characterizing Graphitic Carbon with X-ray Photoelectron Spectroscopy: A Step-by-Step Approach. *ChemCatChem* **2015**, *7*, 2871−2881.
(49) Liu, L.; Zhai, J.; Zhu, C.; Gao, Y.; Wang, Y.; Han, Y.; Dong, S. One-Pot Synthesis of 3-Dimensional Reduced Graphene Oxide-Based Hydrogel as Support for Microbe Immobilization and BOD Biosensor Preparation. *Biosens. Bioelectron.* **2015**, *63*, 483−489.
(50) Aria, A. I.; Gani, A. W.; Gharib, M. Effect of Dry Oxidation on the Energy Gap and Chemical Composition of CVD Graphene on Nickel. *Appl. Surf. Sci.* **2014**, *293*, 1−11.
(51) Osikoya, A. O.; Dikio, C. W.; Ayawei, N.; Wankasi, D.; Afolabi, A. S.; Dikio, E. D. Synthesis, Characterization and Adsorption Studies of Chlorine-doped Carbon Nanotubes. *Adv. Mater. Sci. Appl.* **2015**, *4*, 53−62.
(52) Osikoya, A. O.; Parlak, O.; Murugan, N. A.; Dikio, E. D.; Moloto, H.; Uzun, L.; Turner, A. P.; Tiwari, A. Acetylene-sourced CVD-Synthesised Catalytically Active Graphene for Electrochemical Biosensing. *Biosens. Bioelectron.* **2017**, *89*, 496−504.
(53) Bard, A. J.; Parsons, R.; Jordan, J. *Standard Potentials in Aqueous Solution*; CRC Press: New York, 1985; Vol. 6.
(54) Bard, A. J.; Faulkner, L. R. *Electrochemical Methods, Fundamentals and Applications*, 2nd ed.; Wiley: New York, 2001.
(55) Tiwari, A.; Titinchi, S. *Advanced Catalytic Materials*; Wiley and Sons, 2015.
(56) Parlak, O.; Turner, A. P. F.; Tiwari, A. On/Off-Switchable Zipper-Like Bioelectronics on a Graphene Interface. *Adv. Mater.* **2013**, *26*, 482−486.
(57) Tiwari, A.; Kuralay, F.; Uzun, L. *Advanced Electrode Materials*, John Wiley & Sons, 2016.
(58) Wang, Y.; Guo, Y.; Zhu, G.; Dong, S. Cryoimmobilized Enzyme for Biosensor Construction. *Sens. Actuators, B* **1996**, *31*, 193−196.
(59) Luo, H.; Shi, Z.; Li, N.; Gu, Z.; Zhuang, Q. Investigation of the Electrochemical and Electrocatalytic Behavior of Single-Wall Carbon Nanotube Film on a Glassy Carbon Electrode. *Anal. Chem.* **2001**, *73*, 915−920.
(60) Kalita, G.; Wakita, K.; Umeno, M. Low Temperature Growth of Graphene Film by Microwave Assisted Surface Wave Plasma CVD for Transparent Electrode Application. *RSC Adv.* **2012**, *2*, 2815−2820.
(61) Kibena, E.; Marandi, M.; Sammelselg, V.; Tammeveski, K.; Jensen, B. B. E.; Mortensen, A. B.; Lillethorup, M.; Kongsfelt, M.; Pedersen, S. U.; Daasbjerg, K. Electrochemical Behaviour of HOPG and CVD-Grown Graphene Electrodes Modified with Thick

DOI: 10.1021/acsami.9b01914
ACS Appl. Mater. Interfaces 2019, 11, 11238−11250

Anthraquinone Films by Diazonium Reduction. *Electroanalysis* **2014**, *26*, 2619−2630.
(62) Tiwari, A.; Patra, H. K.; Wang, X. *Advanced Materials Interfaces*; John Wiley & Sons, 2016.
(63) Tiwari, A.; Patra, H. K.; Turner, A. P. F. *Advanced Bioelectronic Materials*; Wiley and Sons, 2016.
(64) Rad, A. S.; Zareyee, D. Adsorption Properties of SO_2 and O_3 Molecules on Pt-Decorated Graphene: A Theoretical Study. *Vacuum* **2016**, *130*, 113−118.
(65) Khosravi, A.; Fereidoon, A.; Ahangari, M. G.; Ganji, M. D.; Emami, S. N. First-Principles vdW-DF Study on the Enhanced Hydrogen Storage Capacity of Pt-Adsorbed Graphene. *J. Mol. Model.* **2014**, *20*, 2230−2236.
(66) Zhang, H.-p.; Luo, X.-g.; Lin, X.-y.; Lu, X.; Leng, Y. Density Functional Theory Calculations Of Hydrogen Adsorption on Ti-, Zn-, Zr-, Al-, And N-Doped and Intrinsic Graphene Sheets. *Int. J. Hydrogen Energy* **2013**, *38*, 14269−14275.
(67) Mazeau, K.; Vergelati, C. Atomistic Modeling of the Adsorption of Benzophenone onto Cellulosic Surfaces. *Langmuir* **2002**, *18*, 1919−1927.
(68) Ergürhan, O.; Parlak, C.; Alver, Ö.; Şenyel, M. Conformational and Electronic Properties of Hydroquinone Adsorption on C_{60} Fullerenes: Doping Atom, Solvent and Basis Set Effects. *J. Mol. Struct.* **2018**, *1167*, 227−231.
(69) Noei, M.; Zolfaghari, F.; Salari, A. A. Hydroquinone Detection by BN Nanotube: DFT Studies. *Int. J. New Chem.* **2014**, *1*, 115−125.
(70) Peyghan, A. A.; Rastegar, S. F.; Hadipour, N. L. DFT Study of NH_3 Adsorption on Pristine, Ni-and Si-Doped Graphynes. *Phys. Lett. A* **2014**, *378*, 2184−2190.

DOI: 10.1021/acsami.9b01914
ACS Appl. Mater. Interfaces 2019, 11, 11238−11250